



Breakup criterion for droplets exposed to the unsteady flow generated by an incoming aerodynamic surface

P. Lopez-Gavilan^a, A. Velazquez^{a,*}, A. García-Magariño^b, S. Sor^b

^a Fluid Mechanics and Aerospace Propulsion Department, Universidad Politécnica de Madrid, Plaza del Cardenal Cisneros 3, 28040 Madrid, Spain

^b National Institute of Aerospace Technology (INTA), 28850, Madrid, Spain

ARTICLE INFO

Article history:

Received 31 July 2019

Accepted 2 January 2020

Available online 8 January 2020

Keywords:

Droplet deformation and breakup

Unsteady flow

Incoming airfoil

ABSTRACT

An experimental and theoretical study is presented on the problem of droplet breakup exposed to a continuously accelerating flow generated by an incoming aerodynamics surface. Droplet breakup experiments were carried out in a rotating arm facility. Droplet diameters were of the order of 1 mm. The maximum velocity of the airfoils located at the end of the rotating arm was 90 m/s. Droplet deformation was computed using a phenomenological model developed previously by the authors. The dynamics of this deformation was coupled to an instability model based on the growth of Rayleigh-Taylor waves at the droplet surface. It was found that, within the experimental uncertainty, breakup occurs when the instability wavelength approaches the droplet hydraulic diameter assuming that it flattens and deforms as an oblate spheroid. This fact allowed for the generation of a theoretical closed-form droplet deformation and breakup model that predicts the onset of breakup with discrepancies of about $\pm 10\%$ when compared to the experimental results. Finally, as an application case, this closed-form model is used to simulate an actual situation in which the objective is to investigate whether a series of droplets that are approached by an airfoil either impact on its surface, or break prior to collision, or break without colliding, or pass through undamaged.

© 2020 Elsevier Masson SAS. All rights reserved.

1. Introduction

The study of droplet deformation and breakup has implications that pertain to the realm of basic Fluid Mechanics and, also, to a very wide spectrum of industrial applications. This could be the reason why experimental, numerical, and theoretical articles on the subject are continuously published in the specialized literature. Specifically, these articles could be broadly classified as those that address the deformation process only, or the breakup process only, or both at the same time.

Regarding the methodologies actually being used, the number of Computational Fluid Dynamics related articles has increased significantly over the past few years. The reason is that recent advances in the numerical modeling of multiphase flows are significant; and this has been translated into a growing interest on the basic physics modeling of droplet related phenomena. On the side of engineering applications, phenomenological models are still much in use because they provide a considerable amount of information at an affordable computational cost. And this is important for industrial design and manufacturing purposes.

In the specific area of aeronautics applications, the study of droplet deformation and breakup is important because, in one way or another, it leads to the fundamental problem of assessing aerodynamic performance under adverse meteorological conditions. Aeronautics flows of interest differ very much from similar flows in other industries. The reason is that in the droplet reference frame, the incoming flow continuously accelerates as the aerodynamics surface (a wing, for example) approaches. This is in contrast with most of other studies in which the incoming flow, as seen from the droplet reference frame, has constant velocity. In practice, this means that experimental facilities dealing with droplet deformation and breakup for aeronautics applications need to be very specific. Typically, rotating arm-like facilities are used for this purpose. Descriptions of this type of facilities could be found in the publications of García-Magariño et al. [1], Sor et al. [2], and Veras-Alba et al. [3].

As mentioned above, the development of a droplet breakup model is important in aeronautics applications because it helps to quantify aerodynamic performance degradation in adverse climate conditions. An extensive review of these effects could be found in the article by Cao et al. [4]. More specifically, the experiments performed by Hansman and Craig [5] have shown that rain with a water content of 30 g/m^3 may degrade the aerodynamic per-

* Corresponding author.

E-mail address: angel.velazquez@upm.es (A. Velazquez).

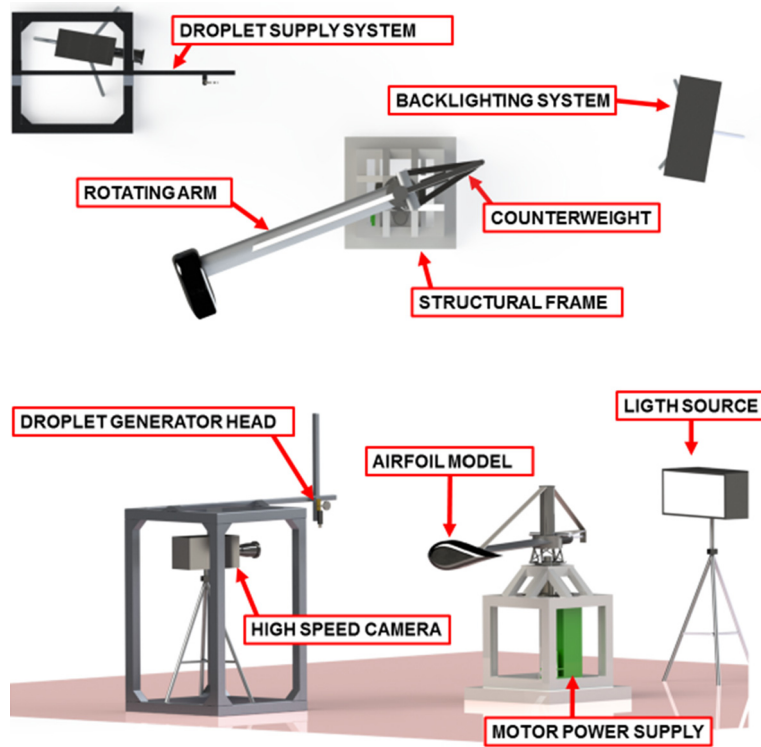


Fig. 1. Sketch of the rotating arm facility. Top: view from above. Bottom: lateral view.

formance of a NACA 64-210 profile by a factor of 15%. Then, it is of interest to develop models that depending on the governing parameters, allow for the prediction of droplet trajectories and eventual breakup of droplets in the vicinity of airfoils. The fact, already mentioned, that the incoming flow, as seen from the droplet reference of frame, is unsteady precludes, in this case, the use of dimensionless numbers (such as, for example, the Weber number) that are meant to describe steady phenomena.

The work described in this study deals with the sequential coupling of a droplet deformation model to a droplet breakup model. In this sense, the present study follows the seminal work of Joseph et al. [6]. In that article, the authors started with the classical Rayleigh-Taylor instability model and ended up with a criterion that linked the growth rate of instability waves to a droplet breakup criterion in the case of constant incoming velocity. Two important aspects that have to do with the developments to be described in the following sections are: a) in their study, Joseph et al. [6] did not account for droplet global deformation, and b) they choose the limiting instability wavelength as the droplet diameter. The comparison between theoretical predictions and experiments was very good, and the authors concluded that the dynamics of breakup is basically controlled by droplet acceleration. A quite different theoretical approach was followed later by Sher and Sher [7]. These two authors proposed an analytical criterion for droplet breakup based on an energy balance that included surface and dissipation energies. Wang et al. [8] considered a droplet deformation model and assumed that droplet breakup occurs when the deformation length reaches some threshold value. In this light, a droplet deformation and breakup model based on the virtual work principle has been presented recently by Sichani and Emani [9]. Considering flows generated by airfoils, García-Magariño et al. [10] have proposed a semi-empirical droplet breakup criterion that accounts for the time derivative of the flow velocity as seen from the droplet reference frame. Finally, it is important to mention the study presented by Park et al. [11]. This was, basically, an experimental study on droplet breakup but a significant part of the data

was based on the measured droplet dimensionless acceleration coefficient. Finally, when searching for generic reviews of droplet breakup models, the interested reader is directed to the works of Bhandarkar et al. [12] and Theofanous and Li [13–15].

Even though the present study, and those referenced above, are not CFD related, it is important to mention the CFD based works of Yang et al. [16] and Kékesi et al. [17]. In reference [16] the authors implemented a breakup criterion on their numerical solver based on the wavelength of the most unstable Rayleigh-Taylor wave and its comparison with the cross stream diameter of the flattened droplet. This, again, is conceptually similar to the approach followed by Joseph et al. [6]. Reference [17] is interesting, also, because of the detailed discussion on the issue of droplet breakup characteristic times.

Regarding the organization of the present article, the experimental facility is described first. Then, the deformation model, the breakup model, and the criterion that links them both are presented and discussed. Results are given next, and a practical application case is described for illustration purposes. Finally, conclusions are presented.

2. Description of the experimental setup

The experimental part of this study was carried out using INTA's rotating arm facility. The mechanical unit is made up of a structural frame, a DC electric motor and a rotating arm. The height of the structural frame is 1.15 m. The electric motor is placed inside with its axle set vertically, and it is connected to the rotating arm by means of a belt drive. The rotating arm, manufactured of aluminum with a streamlined cross section, has a length of 2.2 m from the rotation axis to the center of the Styrofoam airfoils that are placed at its end. A counterweight system is placed opposite to the rotating arm to balance the weight. Struts have been installed over the rotating arm and counterweight beams to improve its stiffness. A sketch of the experimental setup is shown in Fig. 1. The electric motor has a rated power of 5 kW that allows the arm to rotate at a maximum speed of 400 rpm for the largest

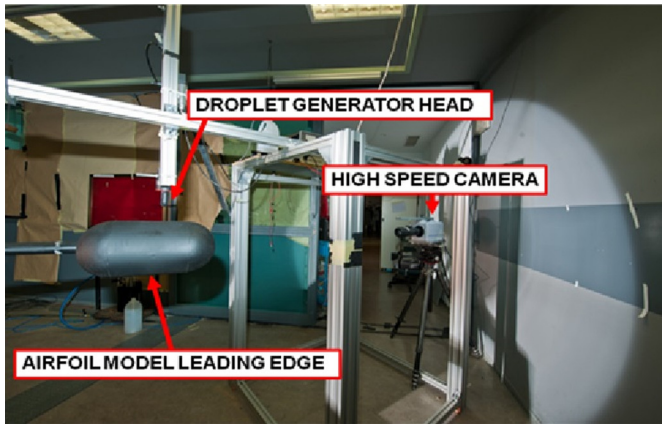


Fig. 2. Actual picture of the facility.

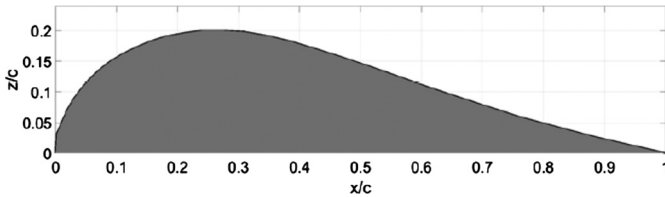


Fig. 3. Upper half of the airfoil cross-section shape.

Table 1
Airfoil dimensionless coordinates.

x/c	z/c	x/c	z/c
0.000	0.000	0.274	0.200
0.002	0.032	0.308	0.198
0.006	0.041	0.344	0.192
0.012	0.055	0.383	0.183
0.020	0.072	0.423	0.171
0.030	0.089	0.465	0.158
0.042	0.105	0.510	0.143
0.056	0.121	0.556	0.127
0.072	0.136	0.604	0.110
0.090	0.150	0.655	0.093
0.110	0.162	0.707	0.076
0.133	0.173	0.762	0.059
0.157	0.183	0.818	0.044
0.183	0.191	0.877	0.028
0.211	0.196	0.937	0.014
0.241	0.200	1.000	0.000

airfoil models. Its rotational speed with an uncertainty of ± 1 m/s is controlled by means of an optical encoder. For the experimental campaigns in this study, three different airfoil speeds were used: 70 m/s, 80 m/s and 90 m/s. A sketch of the facility is presented in Fig. 1. An actual photograph of the system is shown in Fig. 2.

A self-similar symmetric bluff body shape was selected for the airfoil models. Two different airfoil models, M1 and M2, were actually used for the experimental campaigns. Their leading edge radius, chord, and thickness were 0.103 m, 0.690 m and 0.276 m for model M1, and 0.070 m, 0.468 m and 0.187 m for model M2. A view of the airfoil's upper half cross-section is shown in Fig. 3. The airfoil dimensionless coordinates are specified in Table 1.

The air flow in the vicinity of the airfoil leading edge was characterized using the Particle Image Velocimetry (PIV) technique. The room was seeded with atomized olive oil droplets having a diameter of $1 \mu\text{m}$. The flow was illuminated by two synchronized pulsed sheet lasers ND:Yag 190 mJ and recorded by a Power Plus 4MP camera. Three different lenses were used depending on the field of view, a AF-S VR Micro Nikkor 105 mm $f/2.8$ G IF-ED Nano Crystal Coat, a AF Nikkor 80–200 mm $f/2.8$ D IF-ED, and a Nikkor 50

mm $f/1.4$. Vertical and horizontal planes containing the center line of the airfoil were used to define the interrogation windows. Image and laser pulses were synchronized with times between pulses in the range between $1.1 \mu\text{s}$ and $200 \mu\text{s}$. The maximum displacement of the seeding particles between pulses was of the order of 3 mm. This displacement is much smaller than the airfoil leading edge radius that is the characteristic length of the problem. More details about the experimental PIV procedure used to characterize the flow field could be found in references [1,2].

A mono-disperse droplet generator TSI MDG-10 was installed above the rotating plane of the arm so a train of droplets could fall into the path of the airfoil. Droplets were generated by applying an instability (by means of a piezoelectric actuator) to a water jet. The size of the droplets thus generated was controlled by changing the ratio between the flow rate and the harmonic disturbance frequency. In this way, droplets were generated with diameters in the range between 0.4 mm and 1.3 mm. The deformation and motion of the droplets were recorded with a high speed camera Photron SA-5 working at 75,000 frames per second with a maximum resolution of 192×312 pixels. The camera was equipped with a combination of a 200 m Nikkor lens and a 2x teleconverter. A 2000 W xenon backlight was used to increase the contrast between the droplets and the background. The image system setup was calibrated using an AP-G100 grid indexing pattern. A correlation of 14.20 px/mm was found. Images were post-processed using the Photron FASTCAM software. The method proposed by Otsu [18] was used to translate the grey scale images to binary ones. Then, the binary images were used to compute the centroids of droplets which, in turn, were used to track trajectories. The normalized second central moments of the images were used to find ellipses whose minor and major axes fitted the droplet. The method uncertainty, was derived from volume conservation considerations. More details could be found in reference [19]. Relative distances between the droplets and the incoming airfoil were also tracked.

3. Droplet deformation and breakup models

This section is divided into two subsections. First the deformation model is described. This deformation model is, basically, apart from some minor modifications, the one described by the authors in reference [2]. The model is summarized here for the sake of completion. The second subsection addresses the formulation of the breakup model and how the deformation and breakup models are coupled together.

3.1. Deformation model

The following sketch, see Fig. 4, describes the situation that is accounted for by the model.

The experimentally verified hypotheses on which the deformation model is based are as follow:

- The model is valid only in the region close to the airfoil stagnation line. This means that the model does not account for shear effects in the flow field; i.e.: the flow is considered to be one dimensional.
- The model is made up of two equations of motion for the droplet motion dynamics plus another one the droplet deformation.
- The droplet deforms (flattens) as an oblate spheroid.
- Air velocity is much larger than droplet velocity.
- Droplet unsteady drag is made up of two terms: a steady term plus an unsteady one that depends on air velocity time gradients.

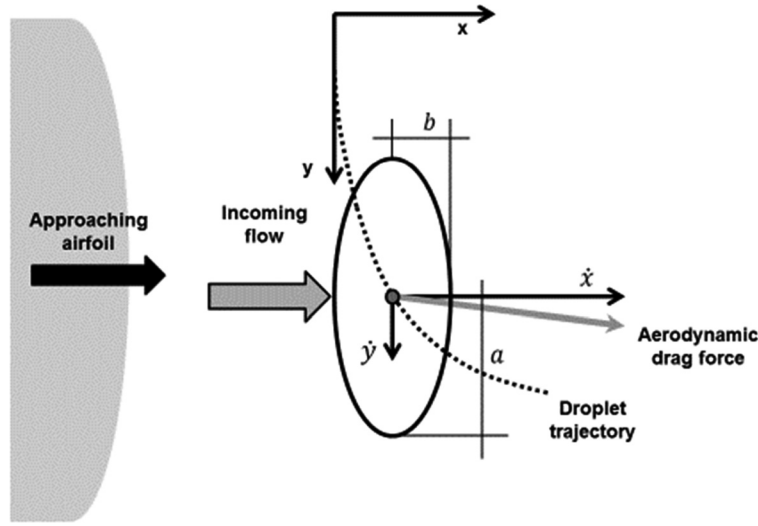


Fig. 4. Sketch showing the basic model setup.

- Droplet deformation rates depend on external pressure force and surface tension effects only; i.e.: viscous effects are considered to be negligible.

Dimensionless model equations are:

$$\frac{d^2\eta}{d\tau^2} = \Pi_1 \mathbb{V}_{sx}^2 \alpha^2 \left[(C_{D_{sphere}}^{(R_d/a)^3} \cdot C_{D_{disk}}^{1-(R_d/a)^3}) + \left(\Pi_2 \frac{1}{\alpha^2 \mathbb{V}_{sx}^2} \frac{d\mathbb{V}_{sx}}{d\tau} \right) \right] \quad (1)$$

$$\frac{d^2\zeta}{d\tau^2} = -\Pi_1 \alpha^2 \mathbb{V}_{sx} \mathbb{V}_{sy} (C_{D_{sphere}}^{(R_d/a)^3} \cdot C_{D_{disk}}^{1-(R_d/a)^3}) + \Pi_3 \quad (2)$$

$$\frac{d^2\alpha}{d\tau^2} = -\Pi_4 \mathbb{F}(\alpha) + \frac{16}{3} \Pi_1 C_p \mathbb{V}_{sx}^2 \quad (3)$$

Equation (1) is the droplet equation of motion along the x axis. Equation (2) is the equation of motion along the y axis. Equation (3) is the droplet deformation equation. Dimensionless variables and functions are defined as follows:

$$\eta = \frac{x}{R_d}, \quad \zeta = \frac{y}{R_d}, \quad \alpha = \frac{a}{R_d}, \quad \tau = \frac{t U_m}{R_c} \quad (4)$$

$$\mathbb{V}_{sx} = \frac{V_{sx}}{U_m}, \quad \mathbb{V}_{sy} = \frac{V_{sy}}{U_m}, \quad \mathbb{A}_d = \frac{A_d}{R_d^2}, \quad \mathbb{F}(\alpha) = \frac{F(a)}{R_d} \quad (5)$$

where x , y and t are the spatial coordinates and time respectively, a is the largest semiaxis of the oblate spheroid (see Fig. 4). U_m is the velocity of the incoming airfoil. R_d and R_c are the initial droplet radius and airfoil leading edge radius respectively. V_{sx} and V_{sy} are the x and y components of the slip velocity, (air velocity minus droplet velocity). Whenever air velocity is much larger than droplet velocity, V_{sx} and V_{sy} can be approximated by the air velocity components relative to the droplet. A_d is the droplet surface area and $F(a)$ is dA_d/da , that is an analytical function. In particular, for an oblate spheroid, the dimensionless surface area \mathbb{A}_d is defined as:

$$\mathbb{A}_d = \frac{A_d}{R_d^2} = 2\pi\alpha^2 + \frac{\pi}{\alpha(\alpha^6 - 1)^{1/2}} \ln \frac{1+e}{1-e} \quad (6)$$

$$e = \frac{(\alpha^6 - 1)^{1/2}}{\alpha^3} \quad (7)$$

The dimensionless parameters that appear in equations (1), (2) and (3) are,

$$\Pi_1 = \left[\frac{3}{8} \frac{\rho_{air}}{\rho_d} \left(\frac{R_c}{R_d} \right)^2 \right] \quad (8)$$

$$\Pi_2 = \frac{k R_d}{R_c} \quad (9)$$

$$\Pi_3 = \frac{g R_c}{U_m^2} \left(\frac{R_c}{R_d} \right) \quad (10)$$

$$\Pi_4 = \frac{16}{3\pi} \frac{\sigma}{\rho_d} \left(\frac{R_c}{U_m R_d} \right)^2 \frac{1}{R_d} \quad (11)$$

where ρ_{air} and ρ_d are the air and water density respectively. g is the gravity constant, and σ the water surface tension. k is an experimental calibration coefficient that was found to be constant (equal to 9) that multiplies the unsteady drag term in equations (1). $C_{d_{sphere}}$ and $C_{d_{disk}}$ are the steady drag of the sphere and disk respectively that are used to interpolate the steady drag term of the droplet. The initial conditions needed to integrate equations (1), (2) and (3) are:

$$\eta(0) = 0, \quad \left(\frac{d\eta}{d\tau} \right)_{\tau=0} = 0 \quad (12)$$

$$\zeta(0) = 0, \quad \left(\frac{d\zeta}{d\tau} \right)_{\tau=0} = \frac{R_c}{R_d} \frac{V_0}{U_m} \quad (13)$$

$$\alpha(0) = 1, \quad \left(\frac{d\alpha}{d\tau} \right)_{\tau=0} = 0 \quad (14)$$

Integration of equations (1), (2), and (3), together with the initial conditions (12), (13) and (14), yields the (x, y) trajectories of the droplet and its deformation. Mass conservation of the deformed droplet after the initial spherical shape implies that deformation is described using just one parameter a (see Fig. 4). Air velocity has been obtained first using Particle Image Velocimetry (PIV) technique in the room where the rotating arm was placed. This was done because accurate air flow characterization is crucial as it affects critically the droplet acceleration which, in turn, governs droplet breakup (as it will be described in the next subsection). However, for the practical resolution and analysis of equations (1), (2) and (3), it is far more practical to have an analytical description of the flow field along the stagnation streamline. The fact that the selected airfoil shape was rather blunt (typical of control surfaces in modern aircraft) suggested that the stagnation

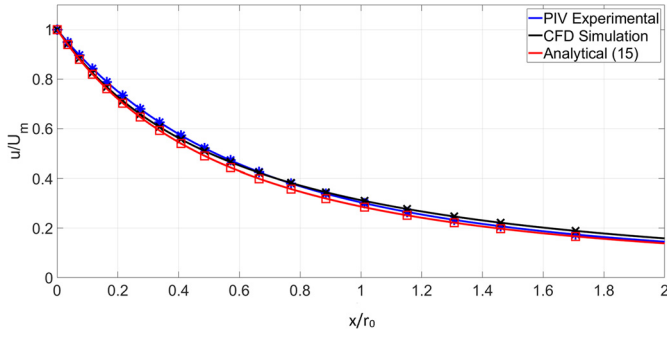


Fig. 5. Incoming flow characterization. Blue line: PIV measurement, black line: numerical simulation, red line: approximate relation (15). (For interpretation of the colors in the figure(s), the reader is referred to the web version of this article.)

streamline could be assimilated to the potential flow past a cylinder with an appropriate coefficient; and this was indeed the case. In particular, it was found that the following analytical expression for the stagnation streamline flow closely matches the air flow actually being measured:

$$V_s = U_m \frac{R_c^n}{(R_c + r_0 - U_m t)^n} \quad (15)$$

where $n = 1.8$ ($n = 2$ in the case of the potential flow around a circular cylinder). r_0 is the initial distance from the droplet to the airfoil leading edge. Fig. 5 shows the comparison between the PIV experimentally measured airflow profile along the stagnation streamline, the results are obtained by performing a 2D numerical inviscid flow simulation using Fluent, and the profile obtained using the approximate relation (15).

3.2. Breakup model and coupling to the deformation model

Joseph et al. [6] performed a stability analysis on the problem of a heavy fluid with a flat surface that falls into a lighter fluid. Basically, they assumed that a disturbance on the flat surface grows as $\exp(nt)$ and found out that:

$$n = \left[\frac{\kappa g(\rho_2 - \rho_1)}{\rho_1 + \rho_2} \right]^{1/2} \quad (16)$$

where subscripts “2” and “1” stand for the heavier and lighter fluid respectively, $\kappa = 2\pi/\lambda$ is the wave number, and λ is the wave length. If surface tension is included into the analysis, it is found that the critical wave number, κ_c , and wavelength, λ_c , are as follows:

$$\kappa_c = \left[\frac{\rho_2 a_c}{\sigma} \right]^{1/2} = \frac{2\pi}{\lambda_c} \quad (17)$$

where a_c is the acceleration of the heavy fluid into the light fluid. If $\lambda < \lambda_c$ the heavy fluid is stable. Now, Joseph et al. [6] made an important assumption. In particular, when dealing with droplets, they assumed that λ_c is the droplet diameter D_d so that if $D_d < \lambda_c$ the droplet is stable (no breakup occurs). Notice, also, that the analysis of Joseph et al. [6] did no account for droplet deformation and considered a constant velocity incoming flow.

Now, two main hypotheses are made in the present work:

- The droplet acceleration in equation (17) is computed from the droplet trajectory and deformation model, equation (1)–(3).
- The critical wavelength in equation (17) that signals the onset of breakup is the hydraulic diameter of the deformed droplet.

The hydraulic diameter of a droplet is defined as:

$$\phi_d = 6 \frac{V_{\text{droplet}}}{A_{\text{droplet}}} \quad (18)$$

where V_{droplet} and A_{droplet} are the droplet volume and surface area respectively. Since the volume of the deforming droplet remains constant until breakup, it is possible to define it as a function of the initial radius:

$$V_{\text{droplet}} = 4/3\pi R_d^3 \quad (19)$$

Combining equations (18) and (19), the hydraulic diameter is written as:

$$\phi_d = 6 \frac{4/3\pi R_d}{A_d/R_d^2} = \frac{8\pi R_d}{A_d} \quad (20)$$

This hydraulic diameter is taken as the critical wavelength that defines the onset of instability (breakup) of the deformed droplet. A_d is the dimensionless surface area of an oblate spheroid previously defined in equations (6)–(7). Naming A_d^* as the A_d value at the onset of instability and replacing it in relation (17) the following relation is obtained:

$$\frac{8\pi R_d}{A_d^*} = 2\pi \left(\frac{\sigma}{\rho_d \ddot{x}^*} \right)^{1/2} \quad (21)$$

where \ddot{x}^* is the droplet horizontal acceleration at the instant of breakup. Rendering relation (21) dimensionless using the scaling described in (4)–(5) the outcome is:

$$\frac{2^4}{(3\pi)^{1/2}} \frac{\ddot{\eta}^{1/2}}{A_d^*} \frac{1}{\Pi_4^{1/2}} = 1 \quad (22)$$

This relation (22) is the breakup criterion actually proposed in this study. Also Π_4 is the dimensionless parameter defined in relation (11). Then, the procedure to predict the onset of breakup is as follows:

- Droplet trajectory and deformation equations (1)–(3) are solved in time starting with initial conditions (12)–(14).
- Ψ (see relation (23)) is continuously monitored during integration of the dynamics equations.

$$\frac{2^4}{(3\pi)^{1/2}} \frac{\ddot{\eta}^{1/2}}{A_d} \frac{1}{\Pi_4^{1/2}} = \Psi \quad (23)$$

- The onset of breakup is defined at the instant when $\Psi = 1$. This instant defines $\ddot{\eta}^*$ and α^* that are the droplet acceleration and droplet deformation at onset of breakup.

Notice that, from an experimental standpoint, the onset of breakup is defined as the instant in which the deformed droplet deviates from the oblate spheroid shape. This is illustrated in Fig. 6 where a frame is presented in which the protrusion around the droplet meridian marks the departure from the oblate spheroid shape.

For large deformations, the droplet hydraulic diameter defined in relation (20) acquires a limiting closed form that simplifies the analysis. This is shown in Appendix A where a simpler form of the breakup criterion (22) is developed in the limit of large deformations.

Table 2

Measured Ψ values at the onset of the droplet breakup. The theoretical model predicts $\Psi = 1$.

Case	R_c (m)	U_m (m/s)	R_d (μm)	Ψ	Case	R_c (m)	U_m (m/s)	R_d (μm)	Ψ
1	0.103	91	597	1.10	22	0.070	91	567	1.18
2	0.103	91	550	1.11	23	0.070	91	558	1.10
3	0.103	91	525	1.10	24	0.070	91	522	1.14
4	0.103	91	450	1.00	25	0.070	91	451	1.06
5	0.103	91	396	0.98	26	0.070	91	403	1.03
6	0.103	91	359	0.95	27	0.070	91	347	1.02
7	0.103	91	302	0.88	28	0.070	91	303	0.95
8	0.103	81	580	1.10	29	0.070	81	606	1.20
9	0.103	81	549	1.04	30	0.070	81	522	1.13
10	0.103	81	485	1.04	31	0.070	81	507	1.20
11	0.103	81	450	1.03	32	0.070	81	450	1.09
12	0.103	81	427	1.03	33	0.070	81	397	1.05
13	0.103	81	348	0.94	34	0.070	81	347	1.04
14	0.103	81	300	0.93	35	0.070	81	296	0.94
15	0.103	71	580	1.05	36	0.070	71	614	1.11
16	0.103	71	551	1.06	37	0.070	71	553	1.16
17	0.103	71	504	1.00	38	0.070	71	514	1.12
18	0.103	71	447	0.99	39	0.070	71	444	1.07
19	0.103	71	402	0.97	40	0.070	71	410	1.08
20	0.103	71	357	0.92	41	0.070	71	347	1.01
21	0.103	71	304	0.88	42	0.070	71	331	1.00

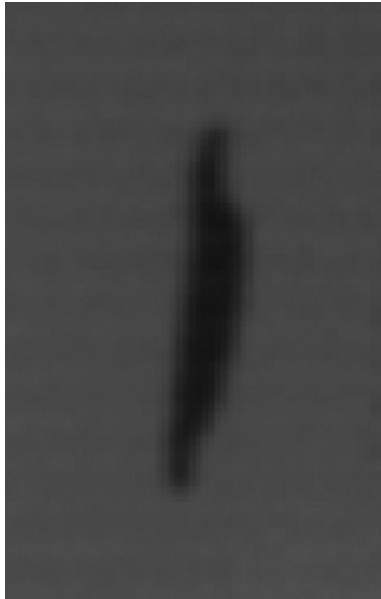


Fig. 6. Actual photograph of the instant (departure from oblate spheroid shape) that is considered as the onset of droplet breakup.

4. Results

The breakup model formulated in equation (22) has been tested in a series of 42 experimental test where the onset of breakup was targeted. Two airfoil leading edge radius: 0.103 m, and 0.070 m, three airfoil velocities: 91 m/s, 81 m/s, and 71 m/s, and seven droplet radii: ranging from about 300 μm to 600 μm , were considered. This makes a total number of $2 \times 3 \times 7 = 42$ cases. The results are presented in Table 2 where the experimentally measured Ψ value for each case is shown. Remember that, according to the breakup analytical criterion (22), Ψ should be 1 at the onset of breakup. Then experimental values of Ψ different than 1 in Table 2 give a direct indication of the discrepancies between experimental and theoretical results.

When analyzing the data provided in Table 2, the following aspects could be noticed:

- The average measured value of Ψ for cases from 1 to 21 ($R_c = 0.103$ m) is 1.01, its standard deviation is 0.071, and the max-

imum and minimum Ψ values are 1.11 and 0.88 respectively. Then, it could be said that measured and predicted values of Ψ agree closely.

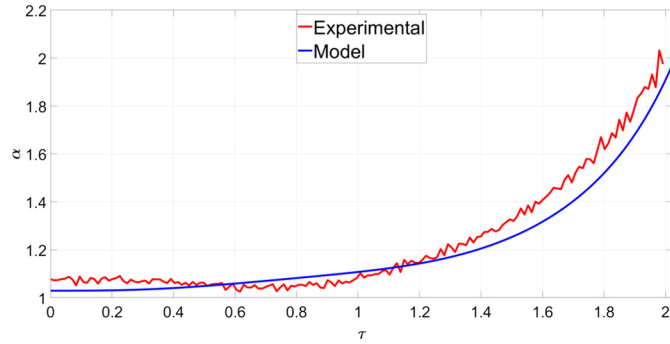
- The average Ψ value of cases from 22 to 42 ($R_c = 0.070$ m) is 1.08 and its standard deviation is 0.075. The maximum and minimum Ψ values are 1.20 and 0.94 respectively. These figures show larger discrepancies than the previous ones (cases 1 to 21). The reason could be that the airfoil in cases 1 to 21 has a leading edge radius of 0.103 m, while in cases 22 to 42 the leading edge radius was 0.070 m. That is: the smaller the airfoil leading edge radius the smaller the region around the stagnation streamline where the flow could be considered one-dimensional, thereby weakening the consistency of the model hypothesis. That is: it is reasonable to expect that smaller airfoil leading edge radius lead to larger discrepancies.
- Within the measurements uncertainty, the breakup model accuracy is not affected by the velocity of the incoming airfoil, i.e.: it is not affected by scale changes in the continuously accelerated flow that impinges on the droplet. This means that the drag term that has been implemented in the droplet trajectory equations (made up of a steady term plus an unsteady one) reasonably models the actual drag effects.
- Typically, the largest discrepancies between model and experimental results occur when the largest droplets are considered. In this regard, it was observed that the larger droplets emitted from the droplet generator had a slight tendency to deviate from the perfect spherical form. Also, some of them were undergoing small shape oscillations as they were falling down through the air and approached the measurement window in the airfoil path. Typically, these droplets had a tendency to break at a time when this deformation was, still, not the one predicted by the model. Given the form of equation (23), this translates into a breakup value of Ψ larger than 1.

The next question to be addressed is the repeatability of the results. To this end, case 2 (the largest airfoil leading edge radius, the highest velocity, and a large droplet) was repeated 9 times. Also case 42 (the smallest airfoil, at the lowest velocity, with the smallest droplet) was repeated 13 times. The results obtained are presented in Table 3. It is to be noticed that these tests could not be repeated exactly with regard to the initial droplet radius. The reason is that it is not possible to control the droplet generator in such a way so as to produce exactly similar droplets. In the original Case 2 the droplet radius was 550 μm . In the repeatability tests,

Table 3

Results of the repeatability tests.

Case	R_c (m)	U_m (m/s)	R_d (μm)	Ψ	Case	R_c (m)	U_m (m/s)	R_d (μm)	Ψ
2A	0.103	91	546	1.10	42A	0.070	71	359	1.05
2B	0.103	91	534	1.06	42B	0.070	71	336	0.96
2C	0.103	91	526	1.08	42C	0.070	71	333	0.95
2D	0.103	91	560	1.12	42D	0.070	71	335	0.98
2E	0.103	91	546	1.10	42E	0.070	71	335	0.87
2F	0.103	91	546	1.06	42F	0.070	71	342	0.99
2G	0.103	91	532	1.04	42G	0.070	71	357	1.00
2H	0.103	91	536	1.12	42H	0.070	71	347	1.01
2I	0.103	91	560	1.09	42I	0.070	71	340	0.96
					42J	0.070	71	339	1.00
					42K	0.070	71	337	0.85
					42L	0.070	71	330	1.00
					42M	0.070	71	342	1.00

**Fig. 7.** Comparison between measured and predicted α values of the deforming droplet as a function on dimensionless time τ for case 2.

droplet sizes ranged from 526 μm up to 560 μm . In the original case 42, the droplet radius was 331 μm . In the repeatability tests, droplet radius varied between 330 μm and 359 μm .

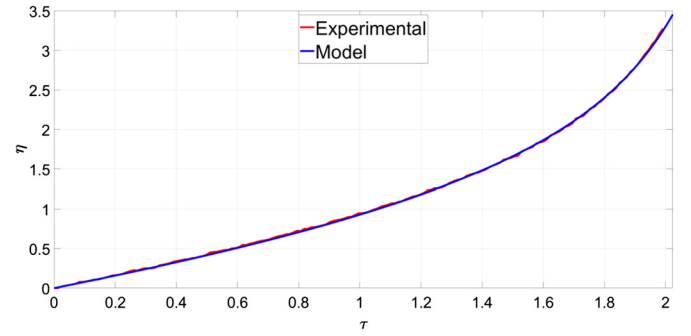
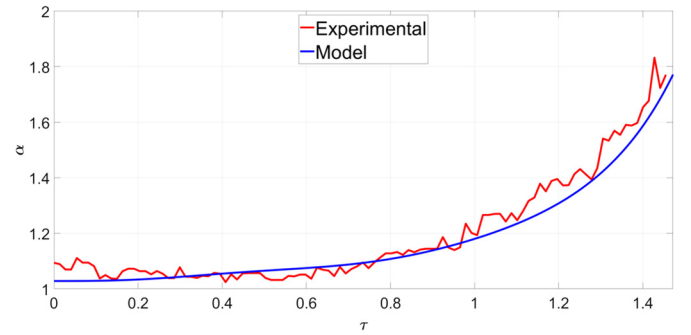
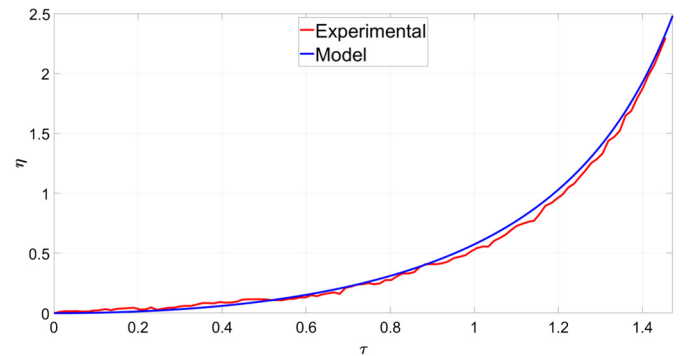
The following aspects could be observed in Table 3:

- In Cases 2A to 2I, the average Ψ at the breakup was 1.09, the standard deviation was 0.028, and the maximum and minimum values were 1.12 and 1.04. So, basically, all repeatability test fit in a band of $\pm 3\%$ around their mean.
- In Cases 42A to 42M, the average Ψ at the breakup was 0.98, the standard deviation was 0.056 and the maximum and minimum values were 1.05 and 0.85. So the repeatability test fit in a band of about $\pm 13\%$ around their mean. Again, this larger band could be caused by the fact that Cases 42A to 42M are further away from the model hypothesis that cases 2A to 2I.

Comparison of results for case 2 in Table 2 are presented in Figs. 7 and 8 respectively. In particular, Fig. 7 shows the comparison between the measured and predicted evolution of α (droplet shape) as a function of the dimensionless time τ . The serrated form of the experimentally measured α evolution has to do with the method (already described) to translate a pattern of pixelated grey shading into an equivalent spheroid shape. Fig. 8 shows the comparison between measured and predicted evolution of the droplet trajectory. Both comparisons shown in Figs. 7 and 8 show a reasonable agreement between experiments and models. The same type of comparison is presented in Figs. 9 and 10 for case 42. In this case, the local discrepancies are larger but the global comparison in terms of the value of Ψ at the onset of breakup is still reasonable.

5. Application case

The application case presented hereafter characterizes the breakup pattern of a series of water droplets placed at different

**Fig. 8.** Comparison between measured and predicted η values of the deforming droplet as a function on dimensionless time τ for case 2.**Fig. 9.** Counterpart of Fig. 7 for case 42.**Fig. 10.** Counterpart of Fig. 8 for case 42.

horizontal positions away from the incoming airfoil. These initial positions are defined by a new dimensionless parameter Π_5 :

$$\Pi_5 = \frac{r_0}{R_c} \quad (24)$$

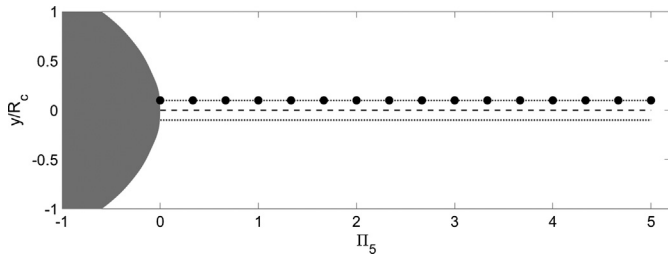


Fig. 11. Sketch of the configuration chosen for the application case.

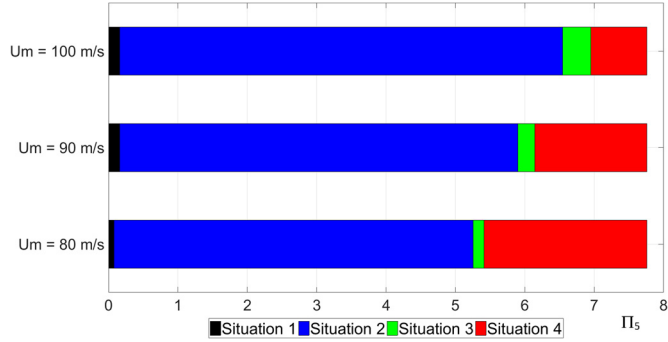


Fig. 12. Predicted droplet situations for three different airfoils velocities as a function on parameter Π_5 .

where r_0 is the initial horizontal distance between the droplet and the airfoil leading edge. Regarding the vertical direction, all droplets are placed initially at a distance of $0.1 R_c$ above the stagnation streamline. Computation is carried out either until the droplet falls at a distance of $0.1 R_c$ below the stagnation streamline, or breaks, or is hit by the airfoil. Fig. 11 illustrates the basic configuration chosen for this application case.

To keep the illustration lighter, only a few droplets have been plotted in Fig. 11. However, the number of actually computed droplets was 100 per case. The residence time t_r of a droplet inside the $\pm 0.1 R_c$ vertical region is $t_r = 0.2 R_c / U_t$, where U_t is the free fall terminal velocity of the droplet (it is assumed that droplets reach the computational region at their free fall terminal velocity). Integration of the model is carried out from $t = 0$ up to $t = t_r$ unless the droplet reaches breakup conditions, or the airfoil touches the droplet. That is, the following situations may occur during integration:

- Situation 1: The residence time t_r of the droplet in the $\pm 0.1 R_c$ vertical region is larger than the time needed for the airfoil to reach the droplet. In this case, the droplet impacts the airfoil in the shape of an oblate spheroid.
- Situation 2: The droplet breaks before it is hit by the airfoil. However, assuming that the centroid of the secondary droplets distribution moves with the same velocity of the original droplet, the airfoil reaches the cloud of secondary droplets before it leaves the $\pm 0.1 R_c$ integration region. In this case, a cloud of secondary droplets impacts the airfoil.
- Situation 3: The droplet breaks before reaching the residence time t_r and leaves the $\pm 0.1 R_c$ integration region without been hit by the airfoil.
- Situation 4: The droplet enters and leaves the $\pm 0.1 R_c$ integration region without either breaking or being hit by the airfoil.

Fig. 12 shows the outcome of three different cases: droplets having an initial radius 0.5 mm being approached by an airfoil with $R_c = 0.103 \text{ m}$ at three different velocities: 100 m/s , 90 m/s , and 80 m/s . The Π_5 parameter (dimensionless initial distance between droplet and airfoil) was varied between 0 and 8.

It could be observed that the proposed method allows for a quantitative prediction of the fraction of droplets that go through one of the four above described situations. For the droplets size and airfoil velocities being considered in this application case, it is found that most of the falling droplets located within a distance of approximately 6 leading edge airfoil radiuses reach breakup condition and impact the airfoil afterwards. The method could easily be adapted to the case where a certain distribution of droplet sizes is used instead of a series of droplets of the same size. The computed fraction of droplets that impact the airfoil (either as a deformed oblate spheroid or as a cloud of secondary droplets) could be used to estimate the deterioration of the airfoil aerodynamics performance.

6. Conclusions

A droplet trajectory and deformation model has been coupled to a droplet breakup model. The objective has been to predict the onset of droplet breakup when an incoming airfoil is approaching. The breakup model is based on an instability analysis that computes the characteristic parameters associated to the growth of disturbances. The main hypothesis that has been made in the model is that the critical wavelength that signals the onset of droplet breakup is the hydraulic diameter of the deformed droplet (assuming that it deforms as an oblate spheroid). This has led to a single analytical relation that is monitored during time integration of the trajectory and deformation droplet dynamics equations. When this relation reaches a certain value, the droplet is assumed to be in breakup conditions.

The theoretical model predictions have been tested experimentally under a variety of conditions in a rotating arm facility. In particular, two airfoil leading edge radiuses: 0.103 m , and 0.070 m , three airfoil velocities: 91 m/s , 81 m/s , and 71 m/s , and seven different droplet radiuses: ranging from about $300 \text{ }\mu\text{m}$ to $600 \text{ }\mu\text{m}$, were considered. For the airfoil with the largest leading edge radius (closer to the model hypothesis) it was found that experimental and model discrepancies in the breakup parameter were of the order of $\pm 10\%$. For the airfoil with the smaller leading edge radius (thereby further away from the hypothesis of the model) discrepancies were of the order of $\pm 20\%$. Uncertainty of the experimental setup was estimated to be of the order of $\pm 10\%$. Repeatability tests were carried out for some representative cases and it was found that, depending on the case, repeated cases fitted within a band of the order of $\pm 3\%$ to $\pm 13\%$ around their mean.

All this means that the proposed model could be used with reasonable confidence when trying to predict what situation is to be encountered by an airfoil that approaches a distribution of droplets (for instance, in the fashion of falling rain). This has been illustrated by presenting an example in which the model predicts what is the fraction of droplets that go through one of the following situations: 1) the spheroidal droplet impacts the airfoil, 2) the droplet breaks up and the ensuing cloud of secondary droplets impact the airfoil afterwards, 3) the droplet breaks up but it is not impinged by the airfoil, and 4) the droplet neither breaks nor it is impinged by the airfoil. Note that situations 1 and 2 have a significant influence on the aerodynamics behavior of the airfoil.

Because of the reasonable agreement that has been found between the theoretical model and the experiments, it could be worth to evolve the model to account for droplets that are not necessarily restricted to be around the airfoil stagnation streamline region. In this case, it would be necessary to account for the shear in the incoming airflow which might lead to rotation of the droplets. This would, possibly, require the introduction of another droplet equation for the rotation dynamics and some changes in the breakup model. If this is to be achieved, it would be possible

predict airfoil aerodynamics performance under rain conditions accounting for the whole region around the airfoil.

Declaration of competing interest

The authors declare no competing interest.

Acknowledgements

This study has been funded by the Spanish Ministry of Economy and Competitiveness (Ministerio de Economía y Competitividad, MINECO) under research contract DPI2016-75296-P. This work is part of the Ph.D. Thesis of the first author, P. Lopez-Gavilan, who has been funded by research grant BES-2017-083024 of the Spanish Ministry of Economy and Competitiveness, MINECO.

Appendix A. Breakup criterion in the limiting case of large deformations

For a sphere, equation (18) is simplified as: $\phi_d = 6(4/3\pi R_d^3)/(4\pi R_d^2) = 2R_d$. The dimensional surface area of an oblate spheroid is:

$$A_d = \pi \left(2a^2 + \frac{b^2}{e} \ln \left(\frac{1+e}{1-e} \right) \right) \quad (\text{A.1})$$

where

$$e = \left(1 - \left(\frac{b}{a} \right)^2 \right)^{1/2} \quad (\text{A.2})$$

In the limit $b \rightarrow 0$, the second term of the equation (A.1) behaves as

$$\lim_{b \rightarrow 0} \pi \frac{b^2}{e} \ln \left(\frac{1+e}{1-e} \right) \rightarrow 0 \cdot \infty \quad (\text{A.3})$$

This needs to be resolved. Renaming $e = (1 - \epsilon)^{1/2}$ and applying L'Hôpital method to the limit (A.3), it is found that

$$\begin{aligned} \lim_{b \rightarrow 0} \pi \frac{b^2}{e} \ln \left(\frac{1+e}{1-e} \right) \\ = \lim_{\epsilon \rightarrow 0} \pi a^2 \frac{\epsilon^2}{(1-\epsilon)^{1/2}} \ln \left(\frac{1+(1-\epsilon)^{1/2}}{1-(1-\epsilon)^{1/2}} \right) \rightarrow 0 \end{aligned} \quad (\text{A.4})$$

So to the first order approximation,

$$A_d \sim 2\pi a^2 \quad (\text{A.5})$$

That means:

$$\phi_d \sim \frac{4/3\pi a^2 b}{2\pi a^2} = 4b \quad (\text{A.6})$$

That is, the critical wavelength that defines the onset of instability (breakup) of the deformed droplet for highly deformed droplets is $4b$ (four times the shortest diameter of the oblate spheroid). Naming as b^* the b value that defines the onset of instabilities and replacing it in relation (17) a new relation is obtained:

$$4b^* = 2\pi \left(\frac{\sigma}{\rho_d \ddot{x}^*} \right)^{1/2} \quad (\text{A.7})$$

By means of using the scaling described in (4)-(5) the relation (A.7) is rendered dimensionless and expressed as

$$\frac{2^3}{3^{1/2} \pi^{3/2}} \frac{\ddot{\eta}^{*1/2}}{\alpha^{*2}} \frac{1}{\Pi_4^{1/2}} = 1 \quad (\text{A.8})$$

In the experiments, the right hand side of relation (A.8) at breakup onset is not “1” but some figure Ψ that differs from “1”.

$$\frac{2^3}{3^{1/2} \pi^{3/2}} \frac{\ddot{\eta}^{*1/2}}{\alpha^{*2}} \frac{1}{\Pi_4^{1/2}} = \Psi \quad (\text{A.9})$$

This relation (A.8) is the simplified breakup criterion for large deformations when $a \gg b$. This simplified criterion has, also, been applied to the 42 cases presented in Table 2. In general, it has been found that theoretical relation (A.8) tends to anticipate the onset of experimental breakup. In the case of the larger airfoil leading edge radius, Ψ varied between 0.98 and 1.18 (as compared to $\Psi = 1$), while in the case of the smaller leading edge radius, Ψ varied between 0.97 and 1.35.

References

- [1] A. García-Magariño, S. Sor, A. Velazquez, Experimental characterization of water droplet deformation and breakup in the vicinity of a moving airfoil, *Aerosp. Sci. Technol.* 45 (2015) 490–500.
- [2] S. Sor, A. García-Magariño, A. Velazquez, Model to predict water droplet trajectories in the flow past an airfoil, *Aerosp. Sci. Technol.* 58 (2016) 26–35.
- [3] B. Veras-Alba, J. Palacios, M. Vargas, C. Ruggeri, T.P. Bartkus, Experimental investigation of supercooled water droplet breakup near leading edge of airfoil, *J. Aircr.* 55 (5) (2018) 1970–1984.
- [4] Y. Cao, Z. Wu, Z. Xu, Effects of rainfall on aircraft aerodynamics, *Prog. Aerosp. Sci.* 71 (2014) 85–127.
- [5] R.J. Hansman, A.P. Craig, Low Reynolds number tests of NACA 64-210, NACA 0012, and Wortmann FX67-K170 airfoils in rain, *J. Aircr.* 24 (8) (1987) 559–566.
- [6] D.D. Joseph, J. Belanger, G.S. Beavers, Breakup of a liquid drop suddenly exposed to a high-speed airstream, *Int. J. Multiph. Flow* 25 (6–7) (1999) 1263–1303.
- [7] I. Sher, E. Sher, Analytical criterion for droplet breakup, *At. Sprays* 21 (12) (2011).
- [8] C. Wang, S. Chang, H. Wu, J. Xu, Modeling of drop breakup in the bag breakup regime, *Appl. Phys. Lett.* 104 (15) (2014) 154107.
- [9] A.B. Sichani, M.D. Emami, A droplet deformation and breakup model based on virtual work principle, *Phys. Fluids* 27 (3) (2015) 032103.
- [10] A. García-Magariño, S. Sor, A. Velazquez, Droplet breakup criterion in airfoils leading edge vicinity, *J. Aircr.* 55 (5) (2018) 1867–1876.
- [11] G. Park, G.S. Yeom, Y.K. Hong, K.H. Moon, Experimental study of time-dependent evolution of water droplet breakup in high-speed air flows, *Int. J. Aeronaut. Space Sci.* 18 (1) (2017) 38–47.
- [12] A. Bhandarkar, P. Manna, D. Chakraborty, Assessment of droplet breakup models in high-speed cross-flow, *At. Sprays* 27 (1) (2017).
- [13] T.G. Theofanous, G.J. Li, On the physics of aerobreakup, *Phys. Fluids* 20 (5) (2008) 052103.
- [14] T.G. Theofanous, V.V. Mitkin, C.L. Ng, C.H. Chang, X. Deng, S. Sushchikh, The physics of aerobreakup. II. Viscous liquids, *Phys. Fluids* 24 (2) (2012) 022104.
- [15] T.G. Theofanous, Aerobreakup of Newtonian and viscoelastic liquids, *Annu. Rev. Fluid Mech.* 43 (2011) 661–690.
- [16] W. Yang, M. Jia, Z. Che, K. Sun, T. Wang, Transitions of deformation to bag breakup and bag to bag-stamen breakup for droplets subjected to a continuous gas flow, *Int. J. Heat Mass Transf.* 111 (2017) 884–894.
- [17] T. Kékési, G. Amberg, L.P. Wittberg, Drop deformation and breakup, *Int. J. Heat Mass Transf.* 66 (2014) 1–10.
- [18] N. Otsu, A threshold method from gray-level histograms, *IEEE Trans. Syst. Man Cybern.* 9 (1) (1979) 62–66.
- [19] A. García-Magariño, S. Sor, A. Velazquez, Data reduction method for droplet deformation experiments based on High Order Singular Value Decomposition, *Exp. Therm. Fluid Sci.* 79 (2016) 13–24.